

SCIENTIFIC REPORTS

OPEN

Pinning and hysteresis in the field dependent diameter evolution of skyrmions in Pt/Co/Ir superlattice stacks

K. Zeissler¹, M. Mruczkiewicz², S. Finizio³, J. Raabe³, P. M. Shepley¹, A. V. Sadovnikov^{4,5}, S. A. Nikitov^{4,5}, K. Fallon⁶, S. McFadzean⁶, S. McVitie⁶, T. A. Moore¹, G. Burnell¹ & C. H. Marrows¹

We have imaged Néel skyrmion bubbles in perpendicularly magnetised polycrystalline multilayers patterned into 1 μm diameter dots, using scanning transmission x-ray microscopy. The skyrmion bubbles can be nucleated by the application of an external magnetic field and are stable at zero field with a diameter of 260 nm. Applying an out of plane field that opposes the magnetisation of the skyrmion bubble core moment applies pressure to the bubble and gradually compresses it to a diameter of approximately 100 nm. On removing the field the skyrmion bubble returns to its original diameter via a hysteretic pathway where most of the expansion occurs in a single abrupt step. This contradicts analytical models of homogeneous materials in which the skyrmion compression and expansion are reversible. Micromagnetic simulations incorporating disorder can explain this behaviour using an effective thickness modulation between 10 nm grains.

It is a truth universally acknowledged, that a thin metallic ferromagnetic/non-magnetic interface in possession of a large spin orbit coupling and thus a strong interfacial Dzyaloshinskii-Moriya interaction (DMI) is in want of the creation of a magnetic Néel skyrmion^{1–3}. Magnetic skyrmions are chiral spin structures which cannot be continuously deformed into another magnetic configuration, such as the ferromagnetic state⁴. Hence, they are topologically stabilised nanoscale structures¹. This stability, their small size (as small as a few nm⁵), and their mobility under spin-torques at low spin current densities^{6–9}, has generated the current research efforts into their usability in novel magnetic information storage technologies.

In the interfacial DMI systems the stabilised skyrmions are of the Néel type. A Néel skyrmion is characterised by the sense of rotation of the spins forming the boundary between the out of plane skyrmion core and the antiparallel surrounding spins. All the boundary spins rotate in a plane perpendicular to the domain boundary. Mathematically, a skyrmion is identified by a non-zero integer winding number S given by¹⁰

$$S = \frac{1}{4\pi} \int \mathbf{m} \cdot \left(\frac{\partial \mathbf{m}}{\partial x} \times \frac{\partial \mathbf{m}}{\partial y} \right) dx dy, \quad (1)$$

where \mathbf{m} is a unit vector pointing along the local magnetisation direction. Here we consider skyrmions with $S = -1$.

Recent experimental advances have showcased the potential of interfacial skyrmions at room temperature for applications^{6,8,9,11–13}. These works pushed the greatly promising results of Fe on Ir(111)³ and PdFe bilayer on Ir(111)^{5,14}, which exhibit nanoscale skyrmions at sub-liquid nitrogen temperatures, a huge step towards practical applications. This was achieved by increasing the operational temperature range to room temperature and

¹School of Physics and Astronomy, University of Leeds, Leeds, LS2 9JT, United Kingdom. ²Institute of Electrical Engineering, Slovak Academy of Sciences, Dúbravská cesta 9, 841 04, Bratislava, Slovak Republic. ³Swiss Light Source, Paul Scherrer Institute, 5232, Villigen, Switzerland. ⁴Laboratory "Metamaterials", Saratov State University, Saratov, 410012, Russia. ⁵Kotel'nikov Institute of Radioengineering and Electronics, Russian Academy of Sciences, Moscow, 125009, Russia. ⁶School of Physics and Astronomy, University of Glasgow, Glasgow, G12 8QQ, United Kingdom. Correspondence and requests for materials should be addressed to K.Z. (email: k.zeissler@leeds.ac.uk)

lowering the necessary stabilisation out of plane field into the mT regime. However, a drawback of these polycrystalline room temperature systems has increasingly become apparent in form of pinning which prevents smooth and reliable skyrmion dynamics^{9,15}.

Theoretically, the effect of pinning on skyrmion motion has been studied in detail^{16–21}. The main conclusion found was that the pinning depends on the skyrmion velocity. At low current densities the skyrmion motion is influenced by pinning in such a way that previously pinned skyrmions remain pinned. However, when studying the same pinning site but in combination with an already moving skyrmion it was observed that the skyrmion moves around the pinning site^{16,18,20}. Furthermore, the Magnus force is expected to help mitigate pinning effects. This is expected to lead to good low current density performance of skyrmions¹⁹. Defects not only influence the motion, pinning also leads to the occurrence of deformation which was observed experimental^{15,22} and theoretical¹⁶.

In a disorder-free system the diameter of a skyrmion shrinks or expands depending on whether a magnetic field is applied antiparallel or parallel to the skyrmion core. The diameter of atomic scale skyrmions, found in a single, defect free, atomic layer of Pd and Fe on Ir(111), roughly scales with the inverse of the applied field $1/\mu_0(H - H_0)$, where $\mu_0 H_0$ is an offset field⁵. This is in agreement with numerical calculations^{23,24}. However, in a pristine system, expansion (and contraction) is in theory perfectly reversible due to the absence of any inhomogeneities that can give rise to pinning. Micromagnetic simulations have shown hysteresis free expansion and contraction when considering pristine ultrathin magnetic layers^{11,13}.

In this paper we are conflating pinning affecting skyrmion translation with pinning affecting skyrmion expansion and contraction. Scanning transmission x-ray microscopy (STXM), utilising x-ray magnetic dichroism (XMCD) contrast, was used to study the magnetic field mediated expansion and compression of skyrmions. It was found that disorder in polycrystalline multilayer systems leads to magnetic pinning. This pinning helps to stabilise skyrmions, however it also leads to a field history dependent hysteresis in the observed skyrmion diameter. Micromagnetic simulation shows that disorder, which induces pinning, can take the form of a spatial modulation in the saturation magnetisation. This represents a spatial thickness fluctuation in real samples. Stochastic pinning is thus a double-edged sword, since the same disorder that leads to a stabilisation of skyrmions also explains the relatively high current density needed to initiate skyrmion motion. Furthermore, the pinning makes quantitative comparison of observed skyrmion spin textures with simulations challenging since the full field history must be taken into account in both cases.

Results and Discussion

Magnetic Characterisation of the Samples. The samples we studied were Pt/Co/Ir multilayers with N repeats, of which a schematic is shown in Fig. 1(a), grown on x-ray transparent silicon nitride membranes by sputtering (see methods section for detail). These were patterned into 1 μm diameter discs for STXM imaging (Fig. 1(b)), whilst sheet films were retained for magnetic characterisation. The out-of-plane easy axis was confirmed with room temperature magneto-optical Kerr effect magnetometry (see Fig. 1(c)). In-plane superconducting quantum interference device vibrating sample magnetometry (SQUID-VSM) (inset in Fig. 1(c)) was used to measure the saturation magnetisation $M_S = 1.2 \pm 0.1$ MA/m, the exchange stiffness $A = 15 \pm 1$ pJ/m, and the effective anisotropy field $\mu_0 H_{\text{Keff}} = 0.90 \pm 0.05$ T (see Fig. 1(d–f)). The exchange stiffness was extracted from the temperature dependence of the saturation magnetisation (see supplementary information for details). The saturation magnetisation was calculated assuming a 0.7 nm cobalt layer in contact with a 0.3 nm layer of proximity-magnetised platinum²⁵ resulting in 1.0 nm of magnetic material separated by 2.5 nm of non-magnetic spacer.

The DMI strength of the $N = 10$ sample was inferred by measuring D on single polycrystalline trilayers. The interfacial DMI is a property of the heavy metal and ferromagnetic material interface, and as such D should not be affected by an increase of $N > 1$. Figure 1(d to f) shows that the three other main magnetic properties, which are material and ferromagnet thickness dependent, are not sensitive to the repetition number N . In particular, the independence of D on the repetition number N is indirectly inferred by measuring effective anisotropy changes with respect to N . The effective anisotropy is an interfacial effect and hence a change in the interface quality as N is increased would result in a change in K_{eff} . No such dependence was observed; K_{eff} is seen to be constant as N is increased (see Fig. 1(e)). This shows that the interface is not significantly altered and a change in D is not expected. Brillouin light scattering (BLS) was used to measure D of a Ta(3.7 nm)/Pt(4.5 nm)/Co(1.0 nm)/Ir(3.0 nm) trilayer. D of the trilayer containing 1.0 nm of cobalt was found to be 0.93 ± 0.07 mJ/m². Using the expected $1/t$ scaling of D a DMI strength of 1.48 mJ/m² was calculated for the 0.7 nm cobalt multilayer stack imaged by STXM. Asymmetric bubble expansion [method as in²⁶] was used to confirm the $1/t$ dependence (see supplementary information).

STXM Imaging. The spin textures in the samples were imaged using XMCD-STXM. An external magnetic field was applied perpendicular to the sample plane. The disc was initially saturated at ± 60 mT and then the field was reversed in incremental steps until a circular bubble was observed (see Fig. 2). The field then was decreased to 0 mT. The bubble remained observable for 18 h after which the disc was saturated using the external magnetic field. In subsequent measurement we have observed bubbles over periods of days. Such a zero field stability was also observed by Pulecio *et al.*¹⁵. The bubble expansion was imaged as the field was reduced stepwise down to 0 mT. The bubble contraction was subsequently observed as the field was increased again. The images in Fig. 2(a–f) show XMCD contrast, extracted from the STXM images, of the disc at different applied magnetic field. The images in Fig. 2(a–c) were taken as the field was increased from 0 mT towards saturation and the images in Fig. 2(d–f) were taken as the field was decreased to 0 mT. Images 2 (b) and (f) were taken at the same field (–20 mT) but show strikingly different skyrmion bubble diameters. From this observation alone it is obvious that the behaviour is not the straightforward reversible process predicted by theory. The diameter evolution, extracted from the XMCD images, under an increasing and decreasing field is summarized in Fig. 2(g) and shows a clear

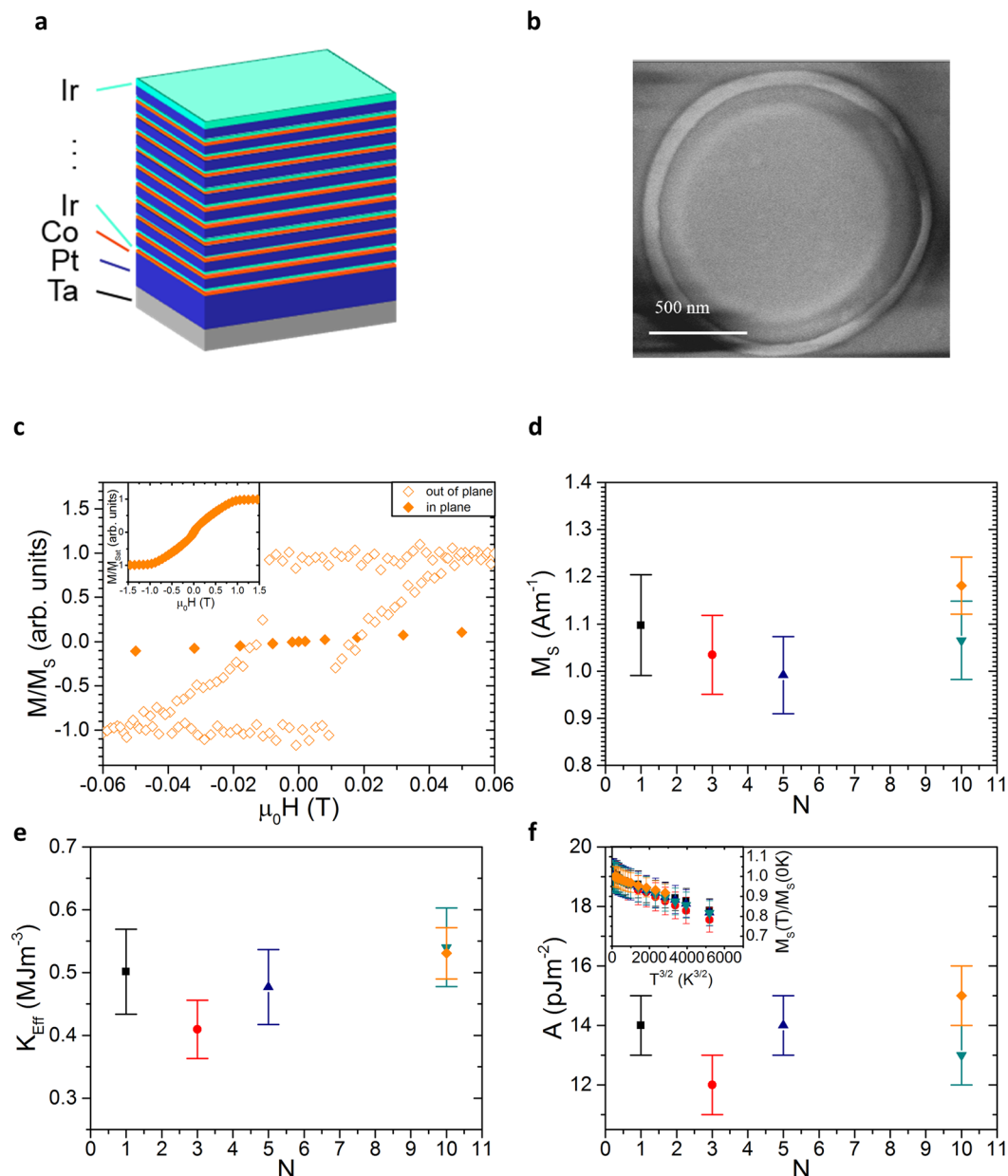


Figure 1. Magnetic properties of $[\text{Co} (0.7 \text{ nm})/\text{Ir} (0.5 \text{ nm})/\text{Pt} (2.3 \text{ nm})]_N$ stacks. **(a)** Schematic of multilayer sputtered for $N = 10$. **(b)** Scanning electron micrograph of a $1 \mu\text{m}$ diameter disc patterned from such a multilayer that was subsequently imaged using STXM. **(c)** Magnetisation versus field showing out-of-plane anisotropy using polar Kerr effect magnetometry and (inset) in-plane SQUID-VSM magnetometry of an unpatterned $N = 10$ multilayer used to pattern nanodisc. **(d)** Saturation magnetisation with respect to number of trilayer repeats N . **(e)** Effective anisotropy and **(f)** exchange constant dependence on repeat number N . The inset in **(f)** shows the linear dependence of the saturation magnetisation (far below from the Curie temperature) on temperature to the power of $3/2$.

hysteretic behaviour. The application of an increasing field leads to a slow shrinking of the skyrmion bubble above $20.0 \pm 0.5 \text{ mT}$. No change in the skyrmion diameter was observed as the magnetic field was reduced until a critical field of $-12.5 \pm 2.5 \text{ mT}$, below which the skyrmion expands abruptly. The diameter changes from $270 \pm 20 \text{ nm}$ at low fields to $130 \pm 20 \text{ nm}$ under fields of several tens of mT. This hysteretic behaviour of the skyrmion size under applied field is explained quantitatively by pinning from the polycrystalline grain boundaries, as introduced in the *Micromagnetic Simulations* section.

A skyrmion shrinks or expands depending on whether a magnetic field is applied antiparallel or parallel to the skyrmion core. The diameter of atomic scale skyrmions, found in a single atomic layer of Pd and Fe on Ir(111), roughly scales with the inverse of the applied field $1/\mu_0(H - H_0)$, where $\mu_0 H_0$ is an offset field⁵. Such epitaxial systems can be assumed to be defect free within the range of the few nm over which the skyrmion occurs. This is in agreement with numerical calculations^{23,24}. Micromagnetic simulations of pristine ultrathin magnetic layers

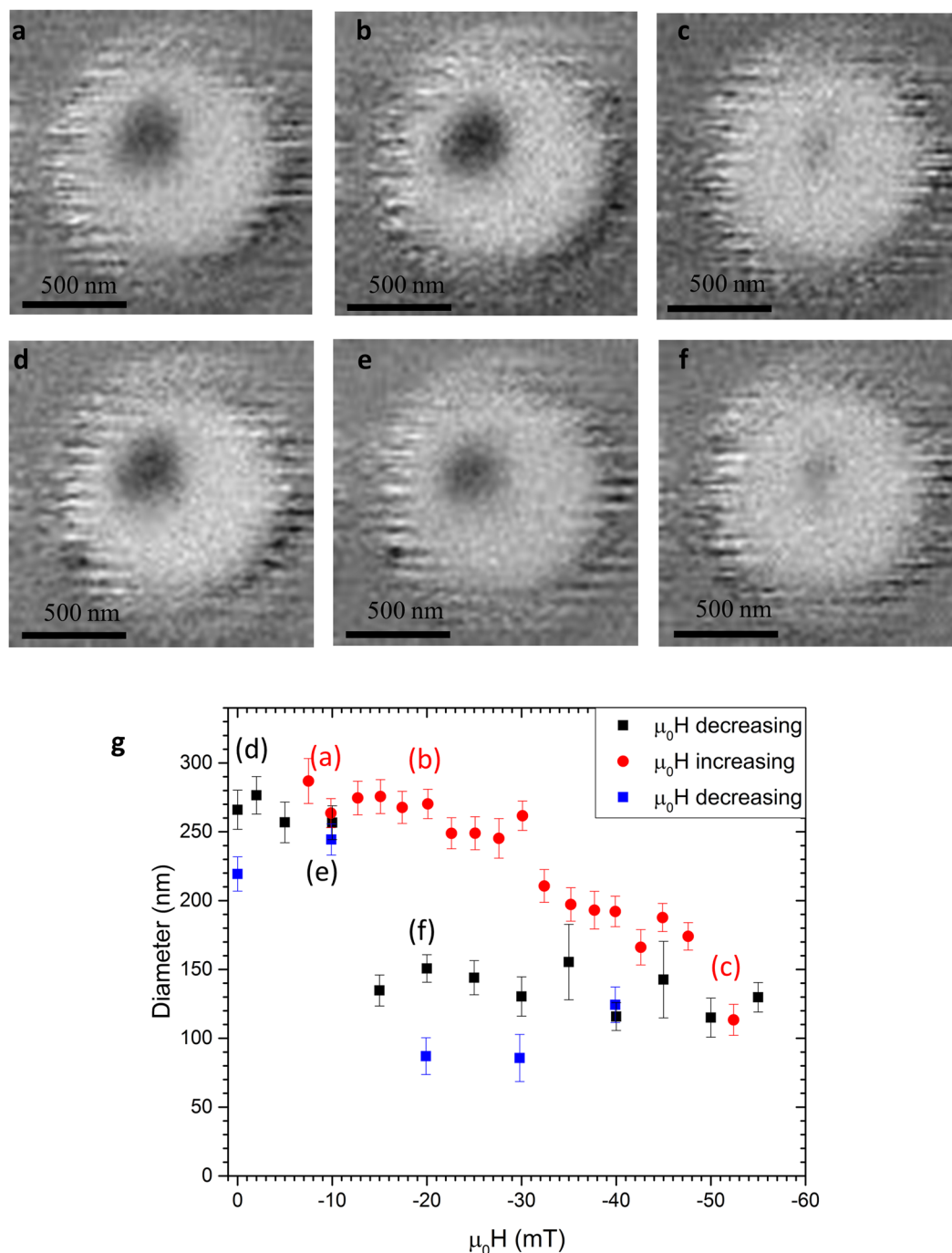


Figure 2. Compression and expansion of a skyrmion in a $[\text{Co} (0.7 \text{ nm})/\text{Ir} (0.5 \text{ nm})/\text{Pt} (2.3 \text{ nm})]_{\times 10}$ multilayer 1000 nm disc imaged using STXM. (a)–(f) show snapshots taken at -10 mT , -20 mT , -52 mT , 0 mT , -20 mT and -10 mT , respectively. Light and dark contrast shows antiparallel out-of-plane magnetized domains. (g) Skyrmion diameter versus applied field with respect to sweep direction. A clear hysteresis can be observed. Letters indicate the points in the hysteresis loop at which the images shown in the earlier panels were acquired.

have also shown similar trends^{11,13}. The hysteretic behaviour is not captured by these models. This comes as no surprise, as disorder changes the local energy landscape that the skyrmion encounters, disrupting the predicted reversibility.

Micromagnetic Simulations. In order to overcome these shortcomings of the above analytical models, we have carried out micromagnetic simulations that reveal that a dependence of the skyrmion diameter on the field history experienced by the disc can only be observed when one introduces disorder. The disorder was introduced in form of a spatial fluctuation in the saturation magnetisation. The disc, comprising 10 layers each of 0.7 nm thickness of ferromagnetic material, was subdivided into grains of average lateral size of 10 nm (using a

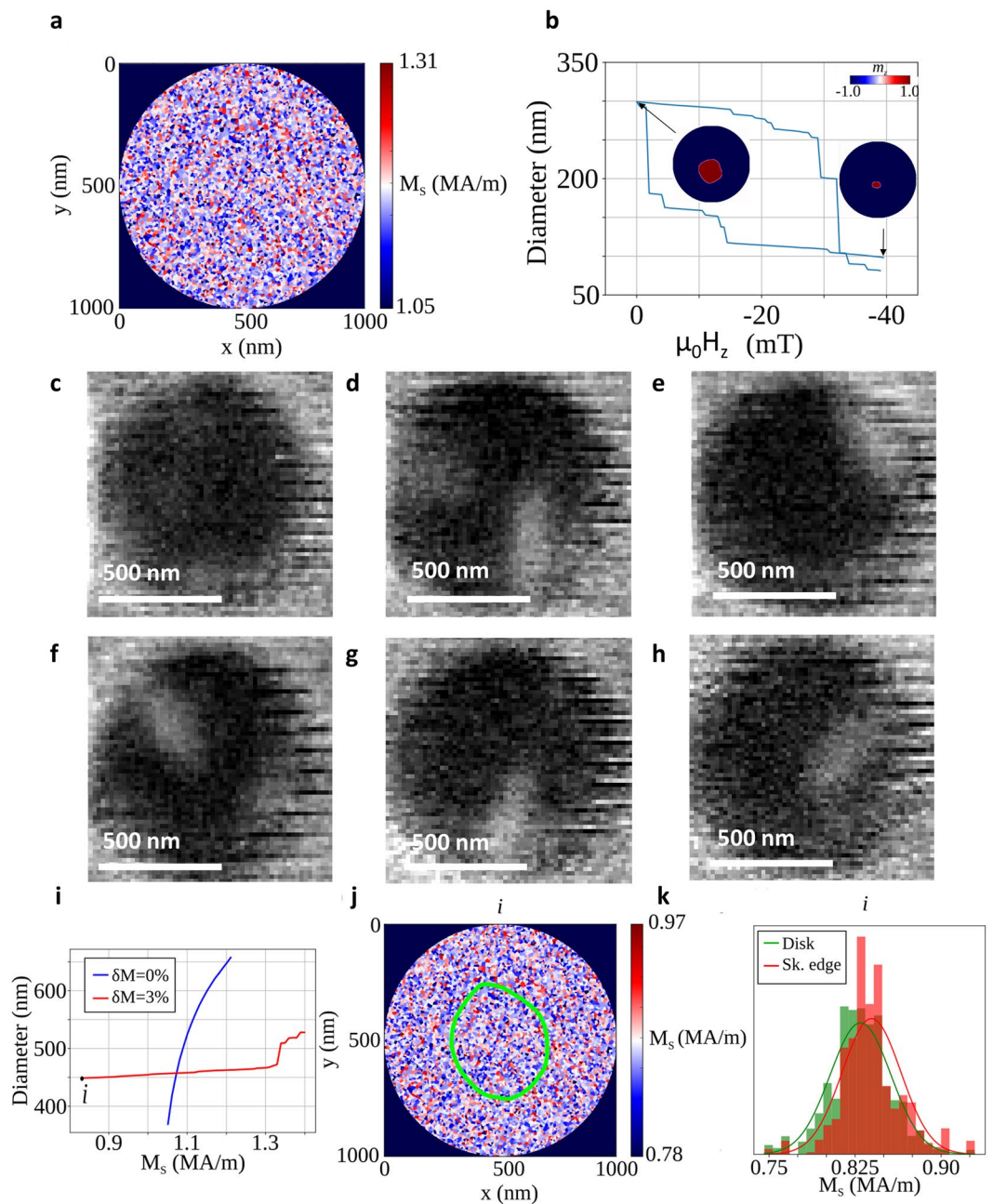


Figure 3. Importance of disorder in magnetic multilayer systems for the formation of skyrmions. **(a)** Grain structure used in the micromagnetic simulations. **(b)** Simulated skyrmion diameter as a function of magnetic field in an $N = 10$ multilayer of 0.7 nm Co layers separated by 2.8 nm spacers. The magnetisation was varied by $\delta M = 3\%$ within grains of average size 10 nm. Insets show the simulated skyrmion shapes at low and high field. **(c–h)** XMCD contrast images of six different 1000 nm discs at 40 mT showing various skyrmion/domain sizes and shapes. **(i)** Simulated skyrmion diameter dependence with changing saturation magnetisation with and without disorder. **(j)** Magnetization distribution in the simulation at point “i” in **(i)**. The boundary of the stabilised skyrmion is marked by the yellow dotted line. **(k)** Magnetisation distribution for the structure at point “i” considering the whole disc (green) and considering only the skyrmion edge grains (red).

2D Voronoi tessellation²⁷). The use of 10 nm grains is discussed in the supplementary information. Each grain was assigned a slightly different saturation magnetisation M_s drawn randomly from a normal distribution centred about a mean value of 1.181 MA/m with a standard deviation of $\delta M_s/M_s = 3\%$ (see Fig. 3(a)). This effectively simulates small thickness variations (roughly 0.1 nm) in the sample (see Fig. 3(a)) (experimentally 2% to 4% variations in the saturation magnetisation could be seen for 0.1 nm variations in the thickness²⁸).

A large skyrmion was stabilised at 50 mT. The field was decreased until the skyrmion was observed to destabilise (around -40 mT) (see Fig. 3(b)). The last stable skyrmion state was then used as the initial state and the field was slowly reduced to 0 mT. A clear hysteretic behaviour of the skyrmion diameter with respect to applied

magnetic field was observed. Simulations (Fig. 3(b)) as well as experimental data (Fig. 2(a,b,d,e) and Fig. 3(c–h)) show a deviation from the typical circular skyrmion shape at low field. The images shown in Fig. 3(c–h) were taken on six separate discs at 40 mT. Simulations confirm the origin of this behaviour to be disorder.

When comparing simulations of pristine discs and of disordered discs, we found that disorder extends the stability of skyrmions well above and below the narrow saturation magnetisation range of a pristine structure (see Fig. 3(i)). In this case, the disc was simulated with a single effective thickness of 7 nm (see supplementary material for a discussion on the validity of this approach). A cell size of $x = 2.0$ nm, $y = 2.0$ nm and $z = 7$ nm was used in order to capture the large skyrmion accurately. Skyrmion stability was observed using a range of mean saturation magnetisation values from 0.83 MA/m to 1.40 MA/m in the disordered disc, but only 1.05 MA/m to 1.21 MA/m in the pristine disc. Point ‘i’ in Fig. 3(i) shows stable skyrmions despite an average saturation magnetisation of 0.825 MA/m, representing an absolute magnetisation range spanning 0.78–0.97 MA/m. When evaluating the skyrmion shape using the last stable condition (labelled as point i in Fig. 3(i)) one finds that the edge of the skyrmion, the domain wall surrounding the bubble, is localised in areas of high magnetisation (see Fig. 3(j and k)). The skyrmion edge is a region of changing magnetisation and as such lowers the magnetostatic energy. Thus the skyrmion edge lowers the magnetostatic energy most efficiently when localised in areas of high saturation magnetisation. This is demonstrated by the shift of the normal distribution in Fig. 3(k) when only considering the grains surrounding the skyrmion edge. This effectively acts as pinning sites in the form of energy wells, whilst grains with low magnetisation act as energy barriers. Therefore, thickness variations throughout the samples affect the pinning distribution, and hence have a direct influence on the skyrmion shape and lead to deformation from the ideal circular shape observed both in simulation and STXM imaging.

However, structural disorder has a direct effect on more than the M_S . It is to be expected that other magnetic parameters, such as the interface anisotropy $K_u = K_{\text{eff}} + \mu_0 M_S^2/2$ (which largely arises at interfaces and so goes as $1/t$), the DMI strength D (also an interface effect with a similar $1/t$ behaviour), and the exchange stiffness A (reduced through finite size effects at these very low thicknesses), will also be affected by it. We have investigated what these potential effects might be in further micromagnetic simulations. In contrast with non-uniformity in M_S and D , where the localisation of skyrmion boundaries pins in regions of higher values, non-uniformity in the anisotropy K_u and A leads to localisation of skyrmion boundaries in regions with lower values, as shown in Fig. 4. Skyrmion boundaries are regions where the magnetisation direction is changing and hence carry an anisotropy and exchange energy penalty. This leads to pinning of the skyrmion edges in areas of low K_u or A grains where this penalty is least. On the other hand the domain wall energy is lowered in regions of high D (the domain wall energy is given by $4(AK_{\text{eff}})^{1/2} - \pi D$). All four of these disorder models (grain-to-grain variations in A , K_u , D , and M_S of $\delta A/A = 10\%$, $\delta K_u/K_u = 10\%$, $\delta D/D = 10\%$, $\delta M_S/M_S = 10\%$ respectively) lead to qualitatively similar behaviour. This is in contrast to small non-uniformity ($\delta K_u/K_u = 1\%$) which has previously been shown to be non-critical to the skyrmion behaviour²⁹. All four are likely to be present in real systems to some extent, and it will be an interesting avenue of future work to determine which is predominant.

Conclusion

In conclusion, disorder, which inevitably occurs in polycrystalline samples, aids skyrmion stability. However, disorder has two implications on the optimisation and characterisation of future devices. Firstly, it makes it difficult to evaluate the DMI strength by the method of comparing observed bubble diameters with simulations, since the disorder and the field-history effects that it gives rise to have to be accurately taken into account. This is especially the case for superlattices with large repeat numbers where the roughness can change as the number of layers is increased³⁰. Disorder and hence pinning has previously been seen to impede device performance resulting in higher than expected current density needed to drive skyrmion motion. A threshold current density of 2×10^{11} Am⁻² was observed by Woo *et al.*⁹ in Co and CoFeB interface systems with 15 repeats. Similar high current densities were measured in (Pt/CoFeB/MgO) \times 15 interface systems⁸. In comparison, single trilayer amorphous materials such as Co₂₀Fe₆₀B₂₀ showed threshold current densities in the order of 1×10^9 A/m². Skyrmions in Pt/Co/Ir systems can manifest with smaller diameters than their counterpart in single trilayer Co₂₀Fe₆₀B₂₀ and hence are more desirable [(30–300 nm)¹³ versus 700–2000 nm⁶]. This shows that achieving a proper understanding of pinning effects is of the utmost importance for the future of skyrmion devices.

Methods

The thin films were deposited by DC magnetron sputtering in a vacuum system with a base pressure of 2×10^{-8} mbar. An argon gas pressure of 3.2 mbar was used during the sputtering and typical growth rates of around 0.1 nm/s were achieved. The superlattice stack, [Co (0.7 nm)/Ir (0.5 nm)/Pt (2.3 nm)] _{$\times N$} , was grown on a seed layer of 4.6 nm Ta/7.2 nm Pt and capped with 1.3 nm of Ir (a schematic shown in Fig. 1(a)). The value of N ranged from 1 to 10. The patterned structures were grown on 200 nm thick Si₃N₄ membranes, with a thin film simultaneously sputtered onto a thermally oxidized Si substrate (with oxide layer thickness of 100 nm) to provide a witness sample for characterisation of material properties. The layer thicknesses were calibrated using X-ray reflectivity on calibration samples sputtered on SiO₂. 1000 nm diameter discs were fabricated using electron beam lithography techniques with a bilayer resist lift-off recipe. The bilayer consisted of diluted copolymer methyl methacrylate (MMA(8.5)MAA) with ethyl lactate (EL11) (4:6 ratio) and a top layer of polymethyl methacrylate (PMMA) 950 A4 was used. Both were spun at 4000 rpm for 40 s and baked at 180 °C for 5 minutes. The pattern was written with a Raith 50 electron beam lithography tool at 30 keV with a 20 μ m aperture in 4 nm steps with an area dosage of 275 μ C cm⁻² and a step size of 6 nm. The disc pattern was developed for 90 s in a 3:7 ratio of deionised water and isopropyl alcohol (IPA) for 90 s and then rinsed with IPA for 30 s. The structures were lifted-off in acetone. Figure 1(b) shows a scanning electron microscopy (SEM) image of a completed disc.

Scanning transmission X-ray microscopy (STXM) at the PolLux (X07DA) beamline at the Swiss Light Source³¹ was used to image the out-of-plane magnetic contrast of the nanodiscs. A Fresnel zone plate with an

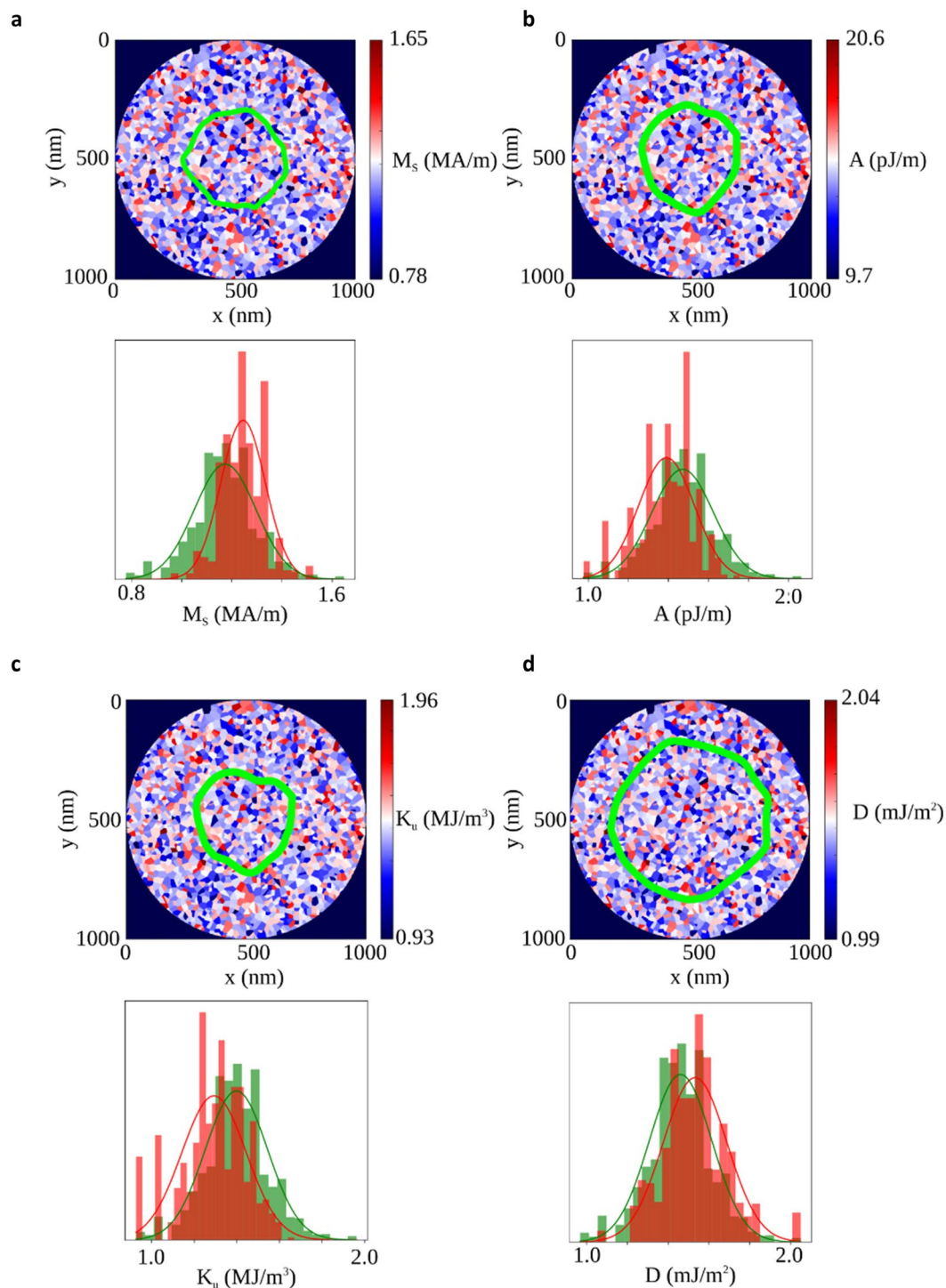


Figure 4. Magnetic parameter disorder in a 7 nm thick Co disc using a 20 nm grain size. **(a)** Saturation magnetisation distribution with $\delta M_s/M_s = 10\%$. **(b)** Exchange stiffness distribution with $\delta A/A = 10\%$. **(c)** Anisotropy constant distribution with $\delta K_u/K_u = 10\%$. **(d)** DMI strength D distribution with $\delta D/D = 10\%$. In all cases the parameter distribution plotted in the histogram over all grains is shown in green and considering only the skyrmion edge grains is plotted in red.

outermost zone of 25 nm was employed to focus the X-rays on the sample, giving a spatial resolution on the order of 30 nm. The images were acquired at room temperature under the influence of a static magnetic field applied perpendicular to the sample surface and parallel to the incident X-rays, which were tuned to the Co L_3 absorption edge (ca. 778 eV). Magnetic contrast was achieved employing the x-ray magnetic circular dichroism effect taking the difference between the absorption of left and right circularly polarized X-rays and dividing it by the sum of the absorption images. This leads to a black and white contrast indicating magnetic moments aligned parallel or

antiparallel to the incident X-rays. The disc was initially saturated at ± 60 mT and then the field was reversed in incremental steps until a circular bubble was observed (see Fig. 2). The field then was decreased to 0 mT. The bubble remained stable and observable. Zero field stability was also observed by Pulecio *et al.*¹⁵. The bubble expansion was imaged as the field was reduced stepwise down to 0 mT. The bubble contraction was subsequently observed as the field was increased again.

The micromagnetic simulation package MuMax³³⁰ was used to simulate the experimental results. The simulations were run in the static regime which calculates energetic minima neglecting dynamic effects. For the hysteretic field dependence simulations, the mesh size and magnetic simulation parameters were chosen to be $x = 2$ nm, $y = 2$ nm, $z = 0.7$ nm. Ten 0.7 nm magnetic layers separated by 2.8 nm were simulated. Periodic boundary conditions along the z axis were used to simulate a finite number of periodic images (macro geometry approach)^{32,33}. For the comparison of pristine and disordered discs, the mesh size was chosen to be $x = 2$ nm, $y = 2$ nm, $z = 7$ nm, and a single layer approach was used with an effective thickness of 7 nm. Further input parameters were as follows: $M_s = 1.181$ MA/m, $K_u = 1.41$ MJ/m³, $A = 14.8$ pJ/m and $D = 1.47$ mJ/m², leading to an exchange length of about 3.3 nm, therefore justifying the discretization grid employed here.

Availability of Data. The data associated with this paper are openly available from the University of Leeds data repository, <http://doi.org/10.5518/261>.

References

- Fert, A., Cros, V. & Sampaio, J. Skyrmions on the track. *Nat Nanotechnol* **8**, 152–156 (2013).
- Fert, A. R. Magnetic and Transport Properties of Metallic Multilayers. *Materials Science Forum* **59–60**, 439 (1990).
- Heinze, S. *et al.* Spontaneous atomic-scale magnetic skyrmion lattice in two dimensions. *Nat Phys* **7**, 713–718 (2011).
- Nagaosa, N. & Tokura, Y. Topological properties and dynamics of magnetic skyrmions. *Nat Nanotechnol* **8**, 899–911 (2013).
- Romming, N., Kubetzka, A., Hanneken, C., von Bergmann, K. & Wiesendanger, R. Field-Dependent Size and Shape of Single Magnetic Skyrmions. *Phys Rev Lett* **114**, 177203 (2015).
- Jiang, W. J. *et al.* Blowing magnetic skyrmion bubbles. *Science* **349**, 283–286 (2015).
- Jonietz, F. *et al.* Spin Transfer Torques in MnSi at Ultralow Current Densities. *Science* **330**, 1648–1651 (2010).
- Litzius, K. *et al.* Skyrmion Hall effect revealed by direct time-resolved X-ray microscopy. *Nat Phys* **13**, 170–175 (2017).
- Woo, S. *et al.* Observation of room-temperature magnetic skyrmions and their current-driven dynamics in ultrathin metallic ferromagnets. *Nat Mater* **15**, 501–+ (2016).
- Braun, H. B. Topological effects in nanomagnetism: from superparamagnetism to chiral quantum solitons. *Adv Phys* **61**, 1–116 (2012).
- Boulle, O. *et al.* Room-temperature chiral magnetic skyrmions in ultrathin magnetic nanostructures. *Nat Nanotechnol* **11**, 449–+ (2016).
- Hrabeč, A. *et al.* Current-induced skyrmion generation and dynamics in symmetric bilayers. *ArXiv* **1611**, 00647 (2016).
- Moreau-Luchaire, C. *et al.* Additive interfacial chiral interaction in multilayers for stabilization of small individual skyrmions at room temperature (vol 11, pg 444, 2016). *Nat Nanotechnol* **11**, 731–731 (2016).
- Romming, N. *et al.* Writing and Deleting Single Magnetic Skyrmions. *Science* **341**, 636–639 (2013).
- Pulecio, J. F. *et al.* Hedgehog skyrmion bubbles in ultrathin films with interfacial Dzyaloshinskii-Moriya interactions. *ArXiv* **1611**, 06869 (2016).
- Kim, J. V. & Yoo, M. W. Current-driven skyrmion dynamics in disordered films. *Appl Phys Lett* **110**, 132404 (2017).
- Iwasaki, J., Mochizuki, M. & Nagaosa, N. Current-induced skyrmion dynamics in constricted geometries. *Nat Nanotechnol* **8**, 742–747 (2013).
- Kim, J. V. & Yoo, M. W. Current-driven skyrmion dynamics in disordered films. *ArXiv* **1701**, 08357 (2017).
- Lin, S. Z., Reichhardt, C., Batista, C. D. & Saxena, A. Particle model for skyrmions in metallic chiral magnets: Dynamics, pinning, and creep. *Phys Rev B* **87**, 214419 (2013).
- Muller, J. & Rosch, A. Capturing of a magnetic skyrmion with a hole. *Phys Rev B* **91**, 054410 (2015).
- Reichhardt, C., Ray, D. & Reichhardt, C. J. O. Collective Transport Properties of Driven Skyrmions with Random Disorder. *Phys Rev Lett* **114**, 217202 (2015).
- Hanneken, C., Kubetzka, A., von Bergmann, K. & Wiesendanger, R. Pinning and movement of individual nanoscale magnetic skyrmions via defects. *New J Phys* **18**, (2016).
- Bogdanov, A. & Hubert, A. The Properties of Isolated Magnetic Vortices. *Phys Status Solidi B* **186**, 527–543 (1994).
- Wilson, M. N., Butenko, A. B., Bogdanov, A. N. & Moncheshy, T. L. Chiral skyrmions in cubic helimagnet films: The role of uniaxial anisotropy. *Phys Rev B* **89**, 094411 (2014).
- Geissler, J. *et al.* Pt magnetization profile in a Pt/Co bilayer studied by resonant magnetic x-ray reflectometry. *Phys Rev B* **65**, 020405 (2002).
- Hrabeč, A. *et al.* Measuring and tailoring the Dzyaloshinskii-Moriya interaction in perpendicularly magnetized thin films. *Phys Rev B* **90**, 020402 (2014).
- Vansteenkiste, A. *et al.* The design and verification of MuMax3. *Aip Adv* **4** (2014).
- Shepley, P. M., Tunncliffe, H., Shahbazi, K., Burnell, G. & Moore, T. A. Tuning domain wall energy with strain: balancing anisotropy and exchange energies in Pt/Co/Ir. *ArXiv* **1703**, 05749 (2017).
- Garcia-Sanchez, F., Sampaio, J., Reyren, N., Cros, V. & Kim, J. V. A skyrmion-based spin-torque nano-oscillator. *New J Phys* **18** (2016).
- Akbulut, S., Akbulut, A., Özdemir, M. & Yildiz, F. Effect of deposition technique of Ni on the perpendicular magnetic anisotropy in Co/Ni multilayers. *J Magn Magn Mater* **390**, 137–141 (2015).
- Raabe, J. *et al.* PolLux: A new facility for soft x-ray spectromicroscopy at the Swiss Light Source. *Rev Sci Instrum* **79** (2008).
- Fangohr, H. *et al.* A new approach to (quasi) periodic boundary conditions in micromagnetics: The macrogeometry. *J Appl Phys* **105**, (2009).
- Fischbacher, T., Franchin, M., Bordignon, G. & Fangohr, H. A systematic approach to multiphysics extensions of finite-element-based micromagnetic simulations: Nmag. *Ieee T Magn* **43**, 2896–2898 (2007).

Acknowledgements

Support from European Union grant MAGICSky No. FET-Open-665095.103 and EPSRC grant EP/M000923/1 is gratefully acknowledged. Part of this work was carried out at the PolLux (X07DA) beamline of the Swiss Light Source. Research has been further co-funded by the EU FP7 SASPRO Programme (REA Grant Agreement Nos 609427, 1244/02/01) and by the Slovak Academy of Sciences. Part of this work was supported by the Grant from Russian Science Foundation (No. 14-19-00760). A.V.S. acknowledges support from the Scholarship of the President of RF (SP-313.2015.5) and Grant of the President of RF (MK-5837.2016.9). The authors are grateful for C. Moutafis for experimental time.

Author Contributions

K.Z. and P.M.S. fabricated the samples. K.Z. did the magnetic characterisation measurements. K.Z., P.M.S., S.F. and J.R. did the STXM imaging. K.Z. and G.B. did the STXM imaging analysis. A.V.S. and S.A.N. did the BLS measurements and analysis. K.F., S.M.c.F. and S.M.c.V. performed the TEM imaging and analysis. M.M. did the micromagnetic simulations and analysis. The manuscript was written by K.Z. and M.M. All the authors reviewed the manuscript. C.H.M. conceived the experiment with T.A.M., G.B. and K.Z.

Additional Information

Supplementary information accompanies this paper at <https://doi.org/10.1038/s41598-017-15262-3>.

Competing Interests: The authors declare that they have no competing interests.

Publisher's note: Springer Nature remains neutral with regard to jurisdictional claims in published maps and institutional affiliations.



Open Access This article is licensed under a Creative Commons Attribution 4.0 International License, which permits use, sharing, adaptation, distribution and reproduction in any medium or format, as long as you give appropriate credit to the original author(s) and the source, provide a link to the Creative Commons license, and indicate if changes were made. The images or other third party material in this article are included in the article's Creative Commons license, unless indicated otherwise in a credit line to the material. If material is not included in the article's Creative Commons license and your intended use is not permitted by statutory regulation or exceeds the permitted use, you will need to obtain permission directly from the copyright holder. To view a copy of this license, visit <http://creativecommons.org/licenses/by/4.0/>.

© The Author(s) 2017